



McKee, J. G., Bevan, R. L. T., Wilcox, P. D., & Malkin, R. E. (2020). Volumetric imaging through a doubly-curved surface using a 2D phased array. *NDT and E International*, 113, [102260].  
<https://doi.org/10.1016/j.ndteint.2020.102260>

Peer reviewed version

License (if available):  
CC BY-NC-ND

Link to published version (if available):  
[10.1016/j.ndteint.2020.102260](https://doi.org/10.1016/j.ndteint.2020.102260)

[Link to publication record in Explore Bristol Research](#)  
PDF-document

This is the author accepted manuscript (AAM). The final published version (version of record) is available online via Elsevier at <https://www.sciencedirect.com/science/article/pii/S0963869519302488?via%3Dihub>. Please refer to any applicable terms of use of the publisher.

## University of Bristol - Explore Bristol Research

### General rights

This document is made available in accordance with publisher policies. Please cite only the published version using the reference above. Full terms of use are available:  
<http://www.bristol.ac.uk/red/research-policy/pure/user-guides/ebr-terms/>

# Volumetric imaging through a doubly-curved surface using a 2D phased array

Jessica G. McKee<sup>1,a)</sup>, Rhodri L. T. Bevan<sup>1</sup>, Paul D. Wilcox<sup>1</sup> and Robert E. Malkin<sup>1</sup>

<sup>1</sup> Department of Mechanical Engineering, University of Bristol, Bristol, BS8 1TR, UK

<sup>a)</sup> Corresponding author: [jessica.mckee@bristol.ac.uk](mailto:jessica.mckee@bristol.ac.uk)

**Abstract.** Ultrasonic phased arrays have become widely used in recent years in non-destructive testing (NDT). However, most NDT arrays are 1-dimensional (1D), which generate 2-dimensional (2D) images from a single position and lack the ability to focus accurately through surfaces that are curved in multiple directions. In this paper, a 2D phased array is used to experimentally image artificial defects (represented by bottom-drilled holes and electrical discharge machined notches) within a test specimen with a doubly-curved surface profile in an immersion configuration. The array is mechanically scanned above the entire surface of the specimen and the 3-dimensional (3D), or volumetric, images generated at each position are combined to produce a single image of the specimen's entire surface. The surface profile is then extracted and discretised for interior volumetric imaging. The results show that the root mean square (RMS) error between the ultrasonically extracted surface and the true surface is 0.04 mm and 95% of absolute errors are less than 0.07 mm. Finally, the positions of visible defects are measured, using (i) the depth above the back wall and (ii) the lateral distance from a notch on the specimen's surface, and compared to their true values. The study shows that the standard deviation of depth and lateral position measurements is 0.68 mm and 0.89 mm respectively. Defects that are located beneath regions of sufficiently steep surface curvature were unable to be imaged.

Keywords: Ultrasound, 2D phased array, volumetric imaging, TFM, FMC

## 1. Introduction

Ultrasonic waves have been utilised in many fields within the past century, such as structural health monitoring (SHM) [1,2] and non-destructive testing (NDT) [3–5]. Developments in NDT over the last few decades have made it possible to obtain accurate internal images of solid structures within the engineering design process, after part manufacture is completed and during service. Ultrasonic imaging involves transmitting a high-frequency pulse (generally in the 1 – 20 MHz range) into a component and processing the reflected signals to generate an image. Detecting and accurately characterising defects within solid structures is an essential part of many procedures to determine structural integrity and remaining component-life.

The use of traditional single-element probes in NDT inspections has many limitations, including the inability to vary focal depth, a restricted number of fixed directions available from which to detect defects, and the consequent potential for missing defects that are in unexpected positions or orientations. Phased arrays can be implemented to overcome some of these problems. Ultrasonic phased arrays are composed of many single-element transducers, and therefore have the benefits of electronic beam steering, focusing and scanning, which are made possible by applying delay laws to individually addressable elements [6]. As a direct result of these properties, phased arrays can be applied to a wider range of imaging scenarios and have the ability to speed up ultrasonic inspections dramatically, along with improving defect image resolution [7]. However, NDT inspections using phased arrays are currently limited to mainly 1-dimensional (1D) arrays with linear elements, and hence only 2-

45 dimensional (2D) slices of a component can be imaged from a single array position. A  
46 substantial limitation of using 1D arrays is that the steering is confined to a single plane and  
47 therefore they are unable to accurately focus through surfaces that are curved in multiple  
48 directions. There is also the possibility of missing scattering effects in the unreconstructed  
49 dimension, which means that there is a chance of missing defects that are in unexpected  
50 positions or orientations. By creating a 2D array with elements distributed across a 2D aperture  
51 it is possible to better characterise defects within components [8]. Similar to how 1D arrays  
52 allow beam steering within a 2D plane, 2D arrays enable beam manipulation throughout a 3-  
53 dimensional (3D) volume without requiring movement of the array. This ability significantly  
54 increases coverage of the imaging region, as long as the array and surface orientations are  
55 favourable, and it allows a more detailed inspection through volumetric beam steering and  
56 focusing [9].

57 Distinguishing between defect types is crucial for thorough and accurate inspections, as the  
58 severity of defects depends on their size, orientation and shape; for instance, it is well known  
59 that planar discontinuities (e.g. cracks) are usually more dangerous than volumetric defects  
60 (e.g. voids) due to their sharp edges that have the potential to grow and cause breaks. Therefore,  
61 obtaining 3D images of defects is desirable for precise defect characterisation. Volumetric  
62 inspections using a 1D array have previously been achieved by translating the array  
63 perpendicular to the 2D imaging plane and combining the resulting images together to  
64 reconstruct a ‘pseudo-3D’ volume from a series of 2D slices [10,11]. However, scattering  
65 effects in the unreconstructed dimension of the individual images are still not captured in this  
66 configuration.

67 A current area of interest in industry is the inspection of defects within regions where the  
68 surface geometry of a component curves in multiple directions, also known as doubly-curved  
69 surfaces, such as those found in pipework branches or nozzles. Current inspection procedures  
70 through these surfaces involve using either (i) a single-element transducer that probes the  
71 region from a range of locations, or (ii) radiographic methods. The use of a single-element  
72 transducer means that a highly-skilled operator needs to interpret the data and it is extremely  
73 challenging to build up a volumetric image of the region; while radiography is not very  
74 effective for detecting and sizing planar defects without prior knowledge of their likely location  
75 and orientation [12]. Due to the double curvature, 1D arrays are not ideal for inspecting through  
76 surfaces of this nature. Hence, the ability of 2D arrays to focus through doubly-curved surfaces  
77 presents a huge opportunity for improving the detection of defects within complex-shaped  
78 components.

79 For non-contact inspections, it is important to correctly account for the surface geometry in  
80 order to maintain a high image quality [13]. There are currently three main approaches to tackle  
81 ultrasonic inspections of this nature. The first of these involves using a liquid, such as water,  
82 to couple a rigid array to the surface of the component under inspection. The liquid acts as an  
83 acoustic couplant between the array and the component. The surface profile can be extracted  
84 from the ultrasonic data using an imaging algorithm [14,15], so previous knowledge of the  
85 surface is not required. In a previous study [16], a 2D array was used to generate 3D images in  
86 immersion; however, in this case the test specimen had a planar surface and determining the  
87 surface position from the data is straightforward. Another approach involves fitting the array  
88 with a wedge that compliments the surface geometry [17], however, each wedge is only suited  
89 to a single, known surface profile and so multiple wedges need to be constructed for the  
90 inspection of a complex component. A lesser-used hybrid method of these two approaches has  
91 also been considered, which involves a membrane-coupled phased array device [18]. The final

92 approach involves the use of a flexible contact array, in which the elements are capable of  
 93 moving in the vertical direction as the array is translated over the surface [19,20].

94 In this paper, experimental defect imaging through a doubly-curved surface using a 2D phased  
 95 array in an immersion setup is investigated. The data-capture format termed Full Matrix  
 96 Capture (FMC) is utilised, along with the post-processing imaging algorithm termed the Total  
 97 Focusing Method (TFM), both of which are explained in [21]. The array is mechanically  
 98 scanned over the entire surface of a test specimen, where FMC datasets are captured at discrete  
 99 overlapping array positions. A combining method (‘stitching’) is then implemented to fuse the  
 100 3D TFM images obtained from each position into a single, larger 3D TFM image. A 3D surface  
 101 extraction method is also presented.

## 102 2. Experimental procedure

### 103 2.1 Array description

104 A 2D sparse array with elements arranged in a Poisson disk formation has been demonstrated  
 105 to outperform a matrix array with the same number of elements, as the non-periodic element  
 106 layout prevents the formation of grating effects while still maintaining a high level of imaging  
 107 resolution [8]. For this reason, a 128-element 2D sparse array with 3 MHz centre frequency is  
 108 used for this work. A description of the array is given in Table 1.

109 Table 1. 2D sparse array parameters.

Array Parameter	Value
Element count	128
Element shape	Circular
Element diameter	1.7 mm
Element pitch	$\geq 1.9$ mm
Element spacing	$\geq 0.2$ mm
Array aperture diameter	30 mm
Centre frequency	3 MHz
-6 dB bandwidth	$\geq 1.5$ MHz

110

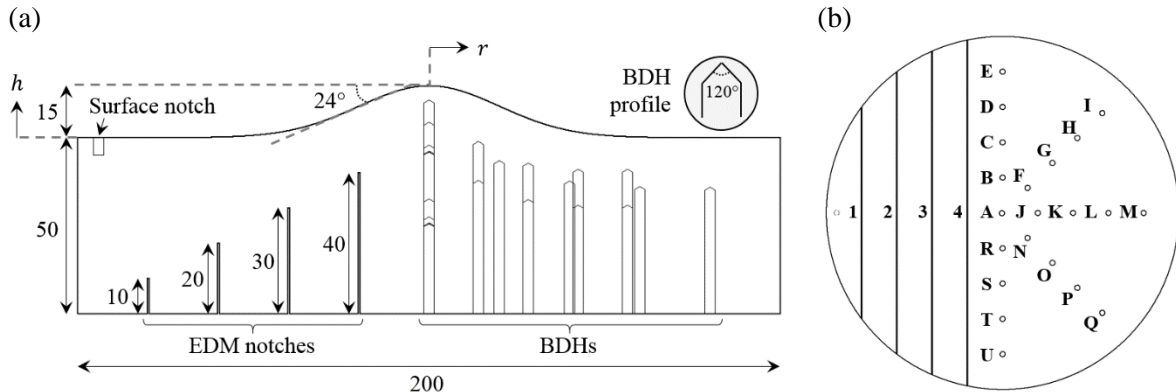
### 111 2.2 Test specimen

112 To represent a doubly-curved surface geometry, an aluminium test specimen with a double-  
 113 curved axisymmetric surface was manufactured, as shown in the side profile in Fig. 1(a). The  
 114 surface was created with a Gaussian profile given by:

$$115 \quad h = h_0 \exp\left(-\frac{r^2}{2\sigma^2}\right) \quad (1)$$

116 where  $r$  is the radial distance from the peak,  $h_0$  is the height of the peak and  $\sigma$  is the standard  
 117 deviation parameter of the Gaussian function. For this specimen,  $h_0$  was 15 mm and  $\sigma$  was 20  
 118 mm, so therefore the steepest angle of inclination on the surface was approximately  $24^\circ$  relative  
 119 to the horizontal. The longitudinal velocity of sound in the specimen,  $v_2$ , was measured to be  
 120 6360 m/s, and hence the wavelength of sound at the centre frequency of the array,  $\lambda_{Al}$ , was 2.1  
 121 mm. 21 bottom-drilled holes (BDHs) were drilled into one side of the base of the specimen,  
 122 with the tip of each hole on each radial arm from the peak at a different depth below the surface;  
 123 the other side of the specimen contained four square electrical discharge machined (EDM)  
 124 notches at different depths. The BDHs were drilled using a standard  $120^\circ$  inclusive drill bit of  
 125 3 mm diameter ( $1.4\lambda_{Al}$ ) and the EDM notches were machined with a wire of 0.5 mm width  
 126 ( $0.2\lambda_{Al}$ ). A bottom-view of the specimen is shown in Fig. 1(b) with each defect labelled. The  
 127 depth of each radial arm below the surface increased from 5 mm (corresponding to the arm

128 containing BDHs A-E) to 25 mm (corresponding to the arm containing BDHs R-U) in 5 mm  
 129 increments. A 3 mm surface notch was drilled into the top surface of the specimen to act as a  
 130 reference point for surface orientation and defect positioning.

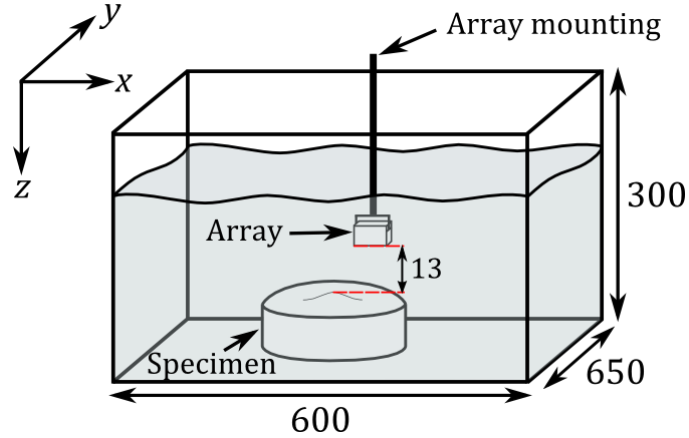


131 **Fig. 1.** Illustration of the designed specimen with machined defects. (a) shows the side profile and (b)  
 132 shows the base view with the defects labelled. Units in mm.

133 The surface was independently measured using a laser scanner and the root mean square (RMS)  
 134 error between the measured surface and that defined by Eq. (1) was found to be 0.06 mm and  
 135 therefore in good agreement. For this reason, the ultrasonically extracted surface will be  
 136 compared directly to the surface defined by Eq. (1).

### 137 2.3 Scanning procedure

138 A scanning tank with three translational degrees of freedom was used in order to perform a 2D  
 139 scan over the entire surface of the specimen. Before scanning, the velocity of sound in water,  
 140  $v_1$ , was measured to be 1470 m/s which corresponded to a wavelength,  $\lambda_W$ , of 0.49 mm. To  
 141 initialise the scan, the specimen was submerged in water and the array was mounted and aligned  
 142 parallel to the back wall of the specimen using a B-scan image obtained over the flat region of  
 143 the surface. The array was then set to a standoff distance of 13 mm above the peak of the  
 144 specimen, before being moved to the scan start location. A schematic diagram of the  
 145 experimental setup is shown in Fig. 2. The total scanned area was 240 mm x 240 mm using a  
 146 total of 225 individual array positions at a pitch of 15 mm in  $x$  and  $y$ , resulting in an array  
 147 aperture overlap of 50% between adjacent positions. The total time to complete the scan was  
 148 approximately 2 hours. Time-data was captured at each position with 10 averages, then filtered  
 149 and Hilbert transformed using a Gaussian window function centred at the array centre  
 150 frequency with a -40 dB half bandwidth of 90% of the array centre frequency.



151

152

153

154

**Fig. 2.** Illustration showing the scanning tank apparatus used to scan the surface of the specimen across the 2D ( $x - y$ ) plane. The standoff between the peak of the specimen and the array was 13 mm. Units in mm.

155

### 3. Image processing methods

156

157

158

159

160

161

162

163

164

165

166

167

Data captured using FMC format contains the time-domain signals (A-scans) of all transmit-receive element pair combinations in the array and enables offline post-processing of the data [21]. TFM imaging is a post-processing algorithm that uses time-domain signals that are stored in FMC format, and generates a fully-focused image by creating an effective focus of the ultrasonic beam at each location in a defined imaging grid. It has been shown that TFM imaging produces high resolution images when compared to other imaging techniques [21] and is hence used throughout this work. As different methods have been used to generate volumetric images in the past, it is worth clarifying that the method described and implemented here involves capturing a single FMC dataset from each array position and stitching all resulting 3D TFM images together. A similar stitching method was used in [14] in the context of 2D imaging using a 1D array, whereby multiple small TFM images with overlapping regions were stitched to produce an image that was larger in size than the individual images.

168

169

170

171

172

173

174

175

176

177

178

179

180

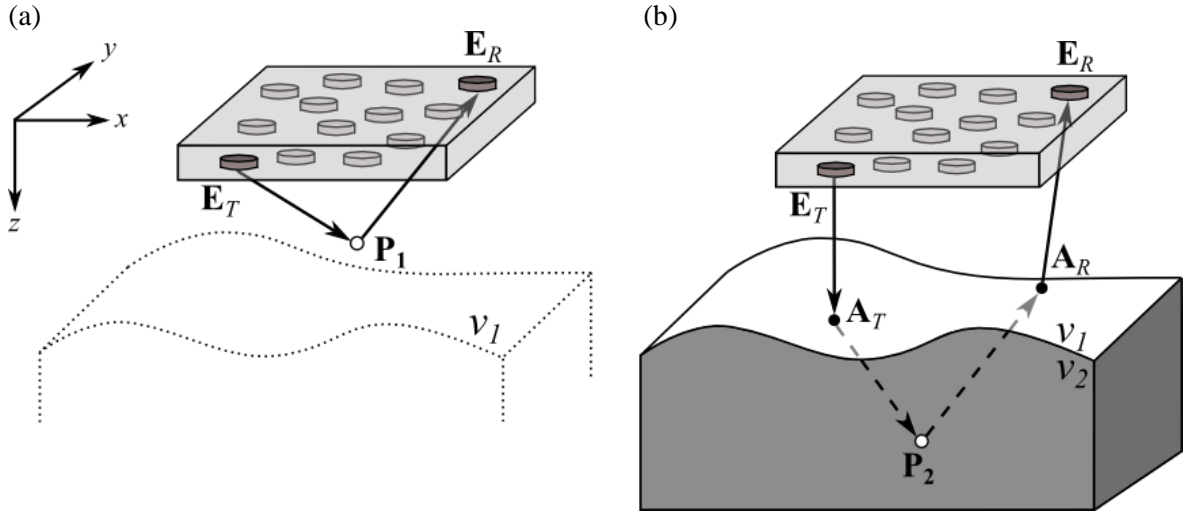
181

182

183

184

TFM imaging is able to synthetically focus ultrasonic signals at every location in an imaging grid by sampling the A-scan corresponding to each transmit-receive element pair at a time that corresponds to the time-of-flight (TOF) of the ray path between the elements and image point. For imaging in a single medium, the TOF is easily obtained through basic trigonometry. An illustration of a ray in single-medium 3D imaging is shown in Fig. 3(a), where the pulse travels between points  $\mathbf{E}_T$ ,  $\mathbf{P}_1$  and  $\mathbf{E}_R$ , which are the position vectors of the transmitting element, image point and receiving element respectively. This journey consists of two ‘legs’, where each leg is a section of the ray path between two points and only  $v_1$  is required to calculate the TOF. The dotted lines in Fig. 3(a) correspond to the surface of the specimen, which is unknown at this stage. The challenge of finding the TOF is harder in the case of dual media with different acoustic velocities, as in the case of immersion imaging. The solution is obtained by using Fermat’s principle of least time [22] to determine the two surface-crossing points that yield the global minimum total TOF between the element pair and each image point. An illustration of the path that results in the minimum TOF between  $\mathbf{E}_T$ ,  $\mathbf{P}_2$  and  $\mathbf{E}_R$  is shown in Fig. 3(b) where  $v_2$  now also needs to be taken into consideration. The path connects the transmitting element  $\mathbf{E}_T$ , to the first surface-crossing location  $\mathbf{A}_T$ , to image point  $\mathbf{P}_2$ , to the second surface-crossing location  $\mathbf{A}_R$  and finally to the receiving element  $\mathbf{E}_R$ .



185 **Fig. 3.** 3D imaging illustration of a ray path in (a) single medium and (b) immersion that yields the  
 186 global minimum TOF between  $E_T$ ,  $P_1$  or  $P_2$ , and  $E_R$  using a 2D phased array. The outline of the  
 187 unknown surface of the specimen is shown by the dotted lines in (a) and plays no part in the  
 188 calculation of the ray path in this case. Solid arrows represent rays travelling in water, while dashed  
 189 arrows represent rays travelling in the specimen.

190 3D TFM imaging through an arbitrary surface in an immersion setup is achieved using a two-  
 191 stage process detailed below.

### 192 3.1 Stage I: Surface extraction

193 The first step to experimentally extract the surface profile of the specimen is to implement a  
 194 single-medium TFM algorithm for each FMC dataset using only  $v_1$ , as shown in Fig. 3(a). The  
 195 location of the surface is unknown at this point and therefore the imaging grid needs to be large  
 196 enough to cover the potential surface region underneath each array position. The surface at  
 197 each position was assumed to be at the location of the first reflection in the time-domain data.  
 198 For an arbitrary image point  $P_1$ , the image intensity,  $I_{surf}(P_1)$ , for each transmit-receive  
 199 element pair is calculated using:

$$200 \quad I_{surf}(P_1) = \left| \sum a_{T,R} h_{T,R} \left( \frac{\|E_T - P_1\| + \|E_R - P_1\|}{v_1} \right) \right| \quad (2)$$

201 where the summation is over all transmit,  $T$ , and receive,  $R$ , element combinations.  $a_{T,R}$   
 202 denotes an optional apodisation term [23] which is unused in this work, hence  $a_{T,R} = 1$ .  
 203  $h_{T,R}(t)$  represents the complex Hilbert transform of the A-scan corresponding to transmitting  
 204 from  $T$  and receiving on  $R$ . Lanczos interpolation of  $h_{T,R}(t)$ , using a kernel size of 3, is utilised  
 205 to sample from the discrete time domain signal and  $\|\cdot\|$  denotes the Euclidean norm of a  
 206 vector.

207 When stitching the image data from all array positions together, the maximum amplitude of  
 208 overlapping image points (i.e. points that were imaged in more than one array position) is taken  
 209 as the true amplitude. Up to this point, no reference is made to the component under inspection  
 210 and the result is a stitched single-medium 3D TFM image of the entire surface of the specimen.  
 211 Due to the complex nature of the specimen's surface and the orientation of the probe relative  
 212 to the surface, there is a variation of reflected surface signal strength. This presents an issue as  
 213 simply taking the points that are above a specified threshold amplitude to define the location  
 214 of the specimen surface results in a discontinuous surface, therefore a more sophisticated, two-  
 215 pass surface extraction process is required. This process is outlined below.

216 A discrete point in the imaging grid is defined as  $\mathbf{P}_{ijk} = (x_i, y_j, z_k)$ , where  $x_i$  denotes equally  
 217 spaced points in  $x$ , and similarly for  $y_j$  and  $z_k$ . The image amplitude at this point is then  
 218 obtained by  $I_{ijk} = |I_{surf}(\mathbf{P}_{ijk})|$ . The first step of the extraction process is to find the indices  
 219  $(i, j, k) = (I, J, K)$  of the location of the maximum amplitude in the stitched TFM image using:

$$220 \quad (I, J, K) = \underset{(i,j,k)}{\operatorname{argmax}} I_{ijk} \quad (3)$$

221 and therefore  $\mathbf{P}_{IJK} = (x_I, y_J, z_K)$  is taken as the first point of the extraction process. Let  $Z_{ij}^{(1)}$   
 222 denote the 3D surface points that are to be determined. The first surface point obtained in  $Z_{ij}^{(1)}$   
 223 is the value of the  $z$  coordinate at the position of the global maximum found above:

$$224 \quad Z_{IJ}^{(1)} = z_K. \quad (4)$$

225 In the first pass, the primary and secondary directions are  $x$  and  $y$  respectively. The 2D ( $x -$   
 226  $z$ ) plane through  $y_J$  is examined first by working out from  $(i, j) = (I, J)$  in the primary  
 227 direction. The next surface point in the  $x$  direction, i.e.  $(i, j) = (I + 1, J)$ , is found by fitting a  
 228 spline,  $S(z)$ , to the image amplitudes,  $I_{(I+1)Jk}$ , at  $k$ -indices that satisfy

$$229 \quad Z_{IJ}^{(1)} - \delta z \leq z_k \leq Z_{IJ}^{(1)} + \delta z, \quad (5)$$

230 where  $\delta z$  is a predefined tolerance parameter, in this case set to approximately  $1.2\lambda_W$ . If the  
 231 maximum of  $S(z)$  exceeds a predefined threshold, then the  $z$  coordinate of the next surface  
 232 point is defined as:

$$233 \quad Z_{(I+1)J}^{(1)} = \underset{z}{\operatorname{argmax}} S(z), \quad (6)$$

234 with the procedure shown in Fig. 4(a). If no value is found in the range of Eq. (5) that satisfies  
 235 the amplitude threshold, the surface point at  $Z_{(I+1)J}^{(1)}$  is defined as absent and the next position  
 236 in the primary direction,  $(i, j) = (I + 2, J)$ , is considered instead. This is repeated until a valid  
 237 point is found. At each absent point the value of  $\delta z$  is slightly increased in case there is a small  
 238 gap in the surface that can be bridged. When a valid surface point is found the process is then  
 239 repeated from Equation (5) starting at that point. This is repeated until 10 consecutive absent  
 240 points are encountered, corresponding to  $6\lambda_W$ , which is assumed to indicate that the edge of  
 241 the measurable surface has been reached. Surface points in the negative  $x$  direction from  $\mathbf{P}_{IJK}$ ,  
 242 i.e.  $(i, j) = (I - 1, J)$ , are then extracted until the other edge of the surface is reached. This  
 243 extraction is shown in Fig. 4(b), where the primary direction is shown by the red arrow and the  
 244 extracted points along the plane are shown by the blue dots.

245 The surface is then extracted in the secondary direction. This is achieved by starting with each  
 246 of the previously extracted surface points in the primary direction and applying the same  
 247 process in the secondary direction. This is shown by the dashed grey arrows in Fig. 4(b) and  
 248  $Z_{ij}^{(1)}$  is now filled with the  $x, y, z$  coordinates of the extracted surface. This concludes the first  
 249 pass of the surface extraction process.

250 In the second pass, the entire extraction process is then repeated, only this time with  $y$  as the  
 251 primary and  $x$  as the secondary direction, as illustrated in Fig. 4(c). This yields a second  
 252 estimate of the surface profile,  $Z_{ij}^{(2)}$ .

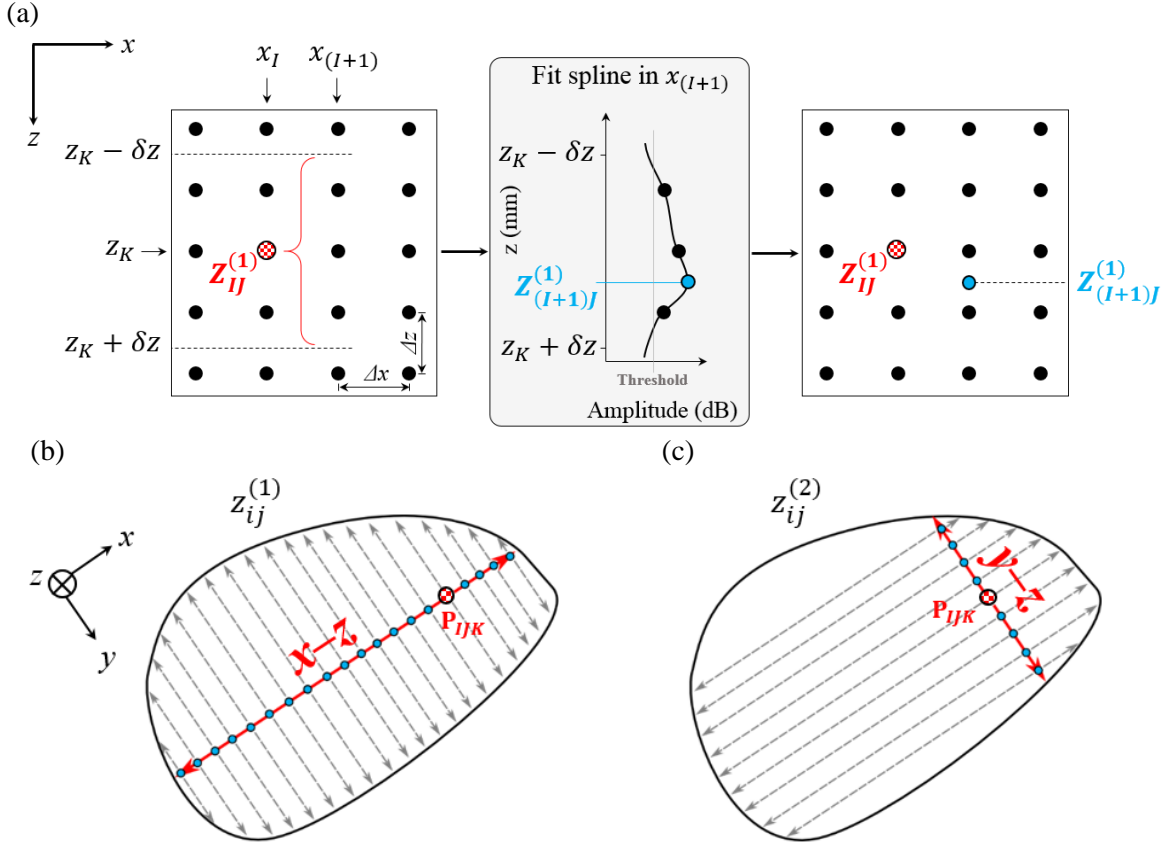
253 The fully-extracted 3D surface,  $Z_{ij}$ , is then found by averaging the two extracted surfaces:



254

$$Z_{ij} = \frac{z_{ij}^{(1)} + z_{ij}^{(2)}}{2}. \quad (7)$$

255 The reasoning behind extracting the surface in two passes is to ensure reliable coverage of the  
 256 surface, independent of the starting point. This would not necessarily be achieved in a single  
 257 pass, as shown by the blank region at the top left of Fig. 4(c).



258 **Fig. 4.** Illustration of the surface extraction method on an arbitrary-shaped surface. (a) Shows the  
 259 process of finding the location of an extracted surface at an adjacent  $x$  position with a  $z$  constraint of  
 260  $\pm\delta z$  applied, where  $\Delta x$  and  $\Delta z$  represent the grid spacing in the  $x$  and  $z$  axes, while (b) and (c) show  
 261 the top view of the extraction directions. In (b) and (c), the red checked dot symbolizes the starting  
 262 point of the extraction process, the blue dots symbolize extracted surface points along the red primary  
 263 extraction direction and the dashed grey arrows show the secondary extraction direction.

264 The extracted surface,  $Z_{ij}$ , is used in the second imaging stage. It was also compared to the true  
 265 surface generated using Eq. (1) to obtain the  $z$  position error at each surface point.

### 266 3.2 Stage II: Interior imaging

267 To image the interior of the specimen, a second set of TOFs are calculated while considering  
 268 the extracted surface points and velocity of sound in each medium, as shown in Fig. 3(b). For  
 269 each array position, a subset of the extracted surface points is considered for TOF calculations  
 270 for computational time and practicality reasons. Only points within a certain distance of the  
 271 vertical line through the centre of the array (i.e. points within a cylinder relative to the array  
 272 axis) are considered. Fermat's principle is applied to determine the surface crossing points and  
 273 TOFs. The TOFs from the extracted surface points to an arbitrary image point,  $\mathbf{P}_2$ , are  
 274 calculated and stored, as are the TOFs from each surface point to an array element,  $\mathbf{E}_\beta$ , where  
 275  $\beta = T, R$ . The surface point,  $\mathbf{A}_\beta$ , corresponding to the global minimum TOF between  $\mathbf{E}_\beta$  and  
 276  $\mathbf{P}_2$  is found, which represents the true ray path from that element in either transmission ( $\beta =$   
 277  $T$ ) or reception ( $\beta = R$ ). By using this result, the intensity of the image,  $I(\mathbf{P}_2)$ , at any image

278 point in the interior imaging grid is calculated by summing over all  $T$  and  $R$  combinations  
 279 using:

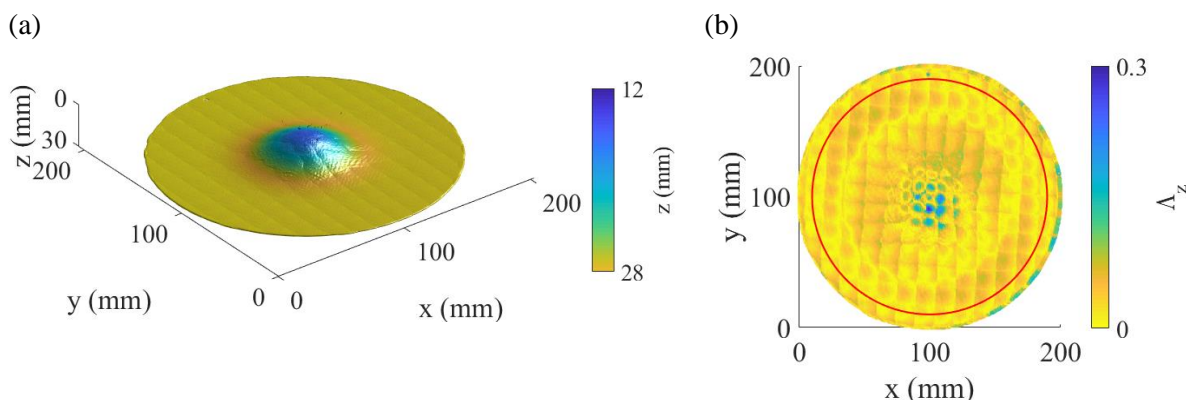
$$280 \quad I(\mathbf{P}_2) = \left| \sum a_{T,R} h_{T,R} \left( \frac{\|E_T - A_T\|}{v_1} + \frac{\|A_T - P_2\|}{v_2} + \frac{\|P_2 - A_R\|}{v_2} + \frac{\|A_R - E_R\|}{v_1} \right) \right| \quad (8)$$

281 where Lanczos interpolation is used to query  $h_{T,R}(t)$  at indiscrte times and  $a_{T,R} = 1$ .

282 All interior TFM images from each array position are then stitched together to create a 3D TFM  
 283 image of the entire interior of the specimen. A summarized outline of the entire imaging process  
 284 is described in the Appendix.

## 285 4. Experimental results

286 The stitched 3D surface TFM image is shown as an isosurface in Fig. 5(a). The isosurface is  
 287 plotted at -10 dB relative to the maximum amplitude and coloured according to depth in the  $z$   
 288 axis. The  $z$  axis represents distance below the array, which was positioned at  $z = 0$  mm. Fig.  
 289 5(b) shows the associated positional error in  $z$ ,  $\Lambda_z$ , between the ultrasonically extracted surface  
 290 and the true surface given in Eq. (1). The RMS error is 0.04 mm, the maximum absolute error  
 291 is 0.3 mm and the surface notch location is evident at  $(x = 100, y = 195)$  mm in Fig. 5(b).

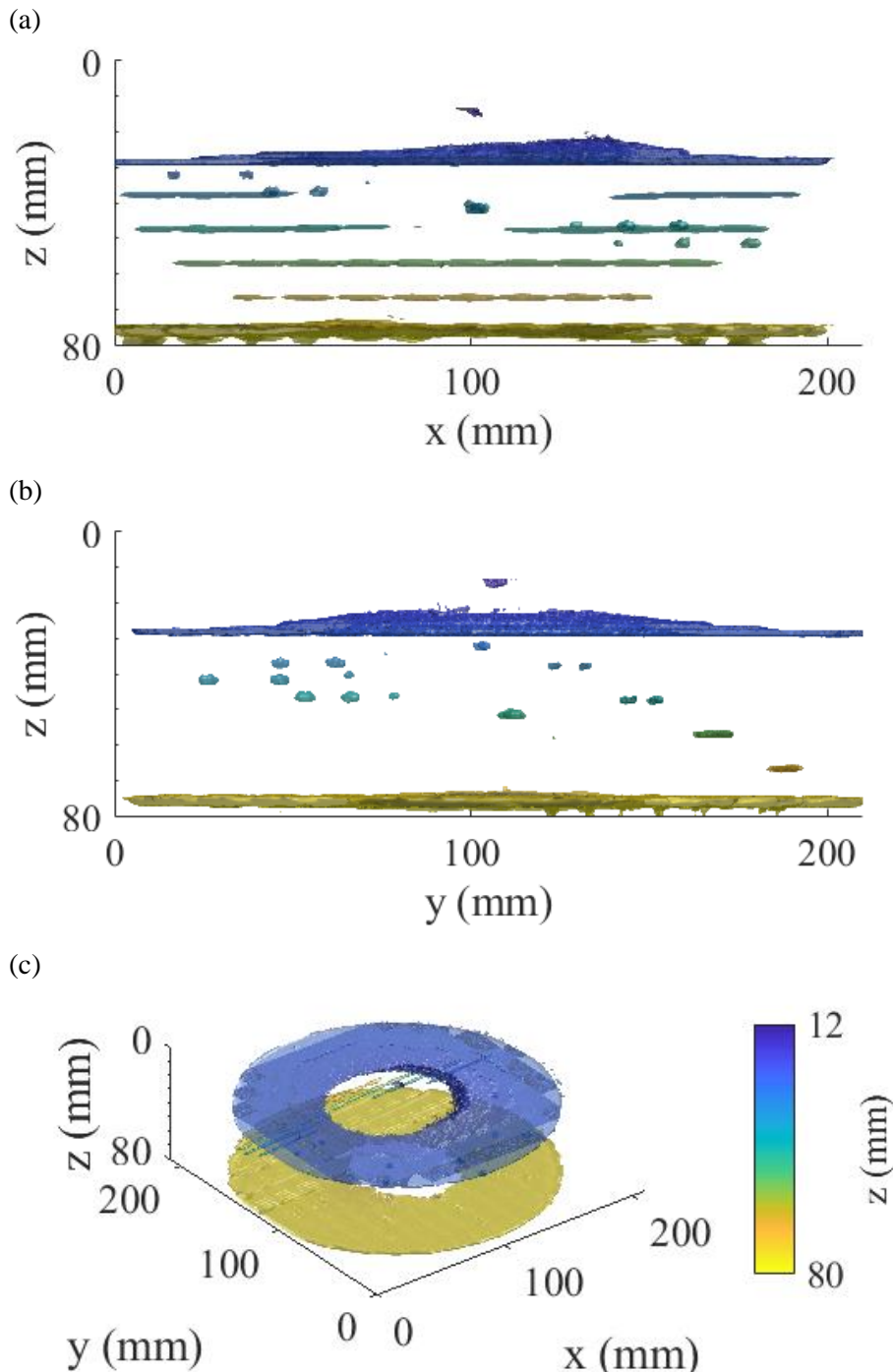


292 **Fig. 5.** (a) The ultrasonically extracted stitched 3D surface TFM image plotted as an isosurface at -10  
 293 dB. (b) Positional error in  $z$ ,  $\Lambda_z$ , between the ultrasonically extracted surface and the true surface  
 294 represented by Eq. (1). Only  $\Lambda_z$  values within a 90 mm radius from the peak in (b), shown by the red  
 295 circle, are considered when calculating the RMS and absolute errors to avoid the errors from the notch  
 296 and edge skewing the results.

297 The stitched 3D interior TFM image of the specimen is shown as an isosurface in Fig. 6, plotted  
 298 at -24 dB relative to, or approximately 6% of, the maximum amplitude in the back wall. By  
 299 windowing the regions around the defects in Fig. 6, individual snapshots of the visible defects  
 300 are obtained and a selection of them are shown in Fig. 7. EDM notches 1 and 4 are shown in  
 301 Fig. 7(a) and (b), while BDHs O, P and Q are shown in Fig. 7(c), (d) and (e) respectively.

302 It was found that the defects located under the region of steep inclination are unable to be  
 303 imaged at any reasonable amplitude level, as is evident by the gap in the isosurface plot of  
 304 EDM notch 4 in Fig. 7(b). For this reason, BDHs B, F, J, N and R are excluded from the results.  
 305 BDH C is also excluded as the signal-to-noise ratio (SNR) is too low for imaging. The central  
 306 location of each BDH and EDM notch was found by taking the mean of the locations of points  
 307 whose amplitudes were greater than or equal to 6 dB below the local maximum amplitude.  
 308 Each defect is plotted at the central location using multiple isosurfaces at different amplitude  
 309 levels relative to the maximum amplitude in the back wall.

310 The positioning of defects is investigated within the specimen and is found using two methods.  
 311 The first involves measuring the depth of each defect above the back wall, and the second  
 312 involves measuring the lateral distance of each defect from the surface notch. These distances  
 313 are then compared to the true values from the specimen design file from Fig. 1, with the results  
 314 shown in Fig. 8(a) and (b) respectively. The standard deviation of depth and lateral distance  
 315 from the surface notch measurements is 0.68 mm and 0.89 mm respectively.

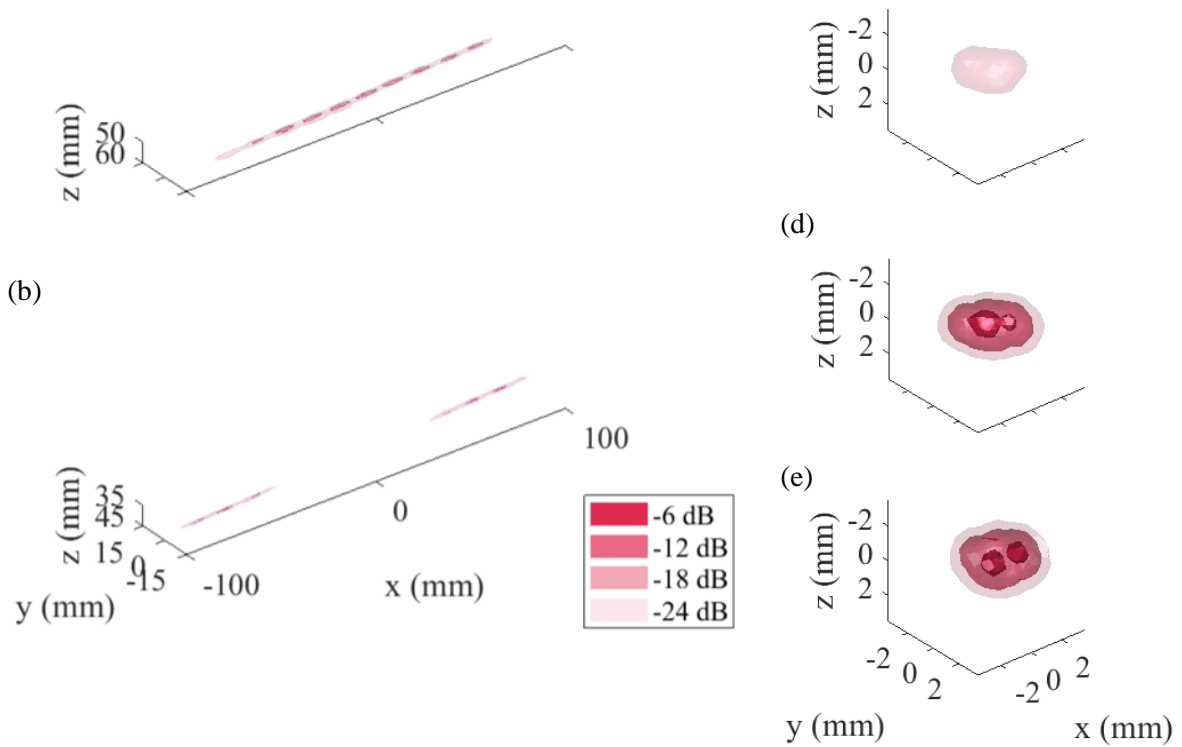


316 **Fig. 6.** Stitched 3D interior TFM image of the specimen plotted as an isosurface at -24 dB relative to  
 317 the maximum amplitude in the back wall and coloured according to distance in z. (a) and (b) show  
 318 elevations, while (c) shows a 3D view.

319

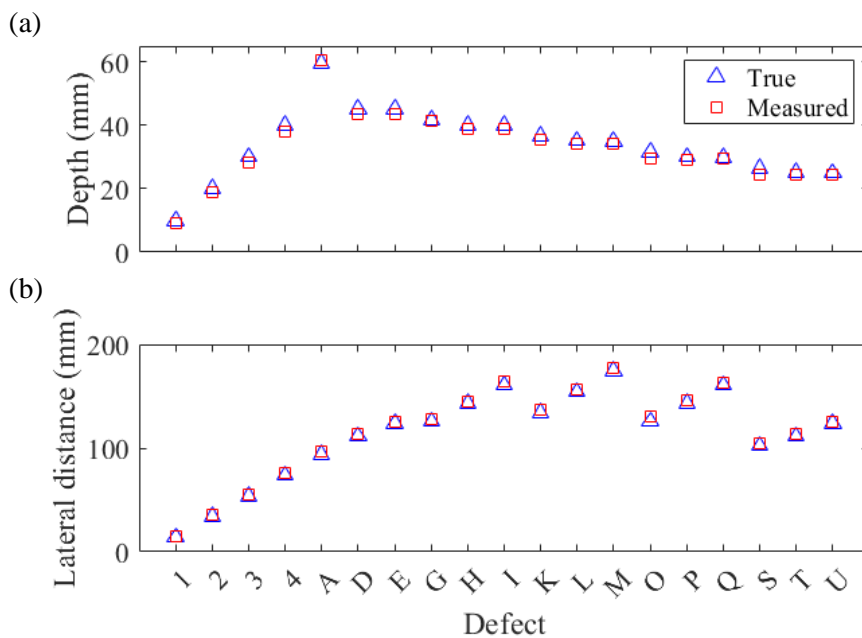
(a)

(c)



320 **Fig. 7.** 3D TFM images of EDM notches (a) 1, (b) 4, and BDHs (c) O, (d) P and (e) Q, plotted as  
 321 multiple isosurfaces at different dB levels relative to the maximum amplitude in the back wall.  
 322 Defects shown at nominal positions.

323



324 **Fig. 8.** Comparison of measured and true defect positions. (a) Shows the comparison of the depth of  
 325 the defects above the back wall of the specimen and (b) shows the comparison of lateral defect  
 326 distance from the surface notch.

## 327 5. Discussion

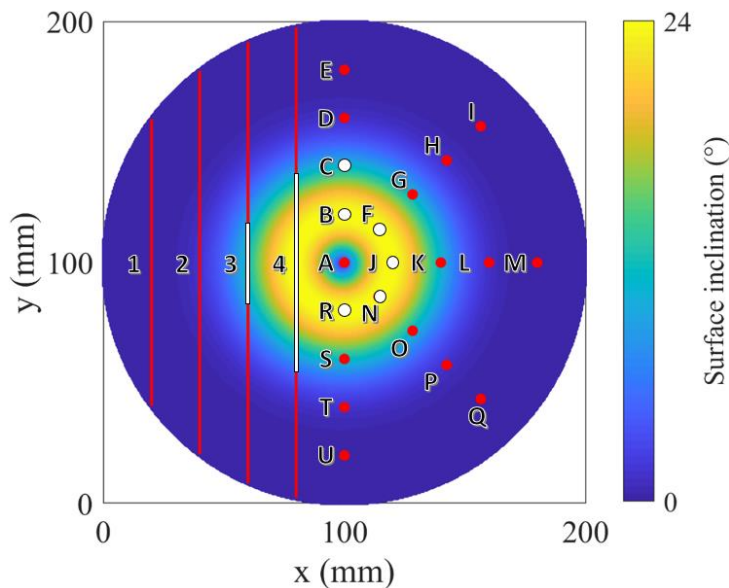
328 The surface extraction algorithm produced a surface that was in close agreement with the  
 329 designed surface, as shown in Fig. 5(b), as 95% of absolute errors between the extracted and  
 330 true surfaces are less than 0.07 mm. The gridded appearance visible in the stitched surface TFM  
 331 in Fig. 5(a) is due to the stitching algorithm, whereby the maximum amplitudes of image points  
 332 in the overlapped regions are taken as the true amplitudes. The  $x$  and  $y$  lengths of the imaging  
 333 region for each array position was twice the diameter of the array, and so the presence of  
 334 imaging artefacts in overlapped regions results in a slightly distorted image. However, applying  
 335 an angle limit during the imaging process would reduce or eliminate artefact appearance.

336 From observing the result in Fig. 6, it is evident that some defects are visible, while others are  
 337 not. The peak of the surface is not visible in Fig. 6 as the isosurface was plotted at a single  
 338 contour level and due to the surface inclination angle and the orientation of the array, the  
 339 amplitude of the inclined surface regions are much lower than that of the flat regions. Defects  
 340 not located directly under the steep inclination region are visible and in the intended locations,  
 341 as evidenced by Fig. 8. Fig. 9 shows the inclination along the surface of the specimen and  
 342 includes the positions of the BDHs and EDM notches. Defects under the region of the surface  
 343 with an approximate inclination larger than the longitudinal critical angle for a wave travelling  
 344 from water to aluminium,  $\theta_c = 13.4^\circ$ , proved impossible to image using this setup orientation.  
 345 EDM notch 4, shown in Fig. 7(b), illustrates this as there is a gap in the isosurface as part of  
 346 the notch is underneath the region of highest inclination. The BDHs that were unable to be  
 347 imaged include BDHs B, F, J, N and R, along with BDH C due to its low SNR and are coloured  
 348 white in the figure. The reason for low SNR on BDH C is due to it lying on the radial arm that  
 349 was drilled at the smallest depth below the surface. The reason for the other defects not being  
 350 imaged is due to several factors. Firstly, consider the surface to be an inclined plane with a  
 351 steepest angle of  $24^\circ$  and the array positioned directly above the steepest surface location. In  
 352 the region of the sample directly under the array, the majority of the incident energy is reflected  
 353 due to the surface angle being larger than  $\theta_c$ . To the side of the array further up the plane, there  
 354 is a region where rays from the array are incident on the surface below  $\theta_c$ . However, the  
 355 directivity amplitude of the elements in the array means that there is low transmission and  
 356 reception sensitivity in these directions as they are at relatively large angles relative to the array  
 357 normal. Fig. 10 shows the directivity,  $D(\phi)$ , of a 1.7 mm diameter circular element radiating  
 358 into water at 3 MHz, calculated using:

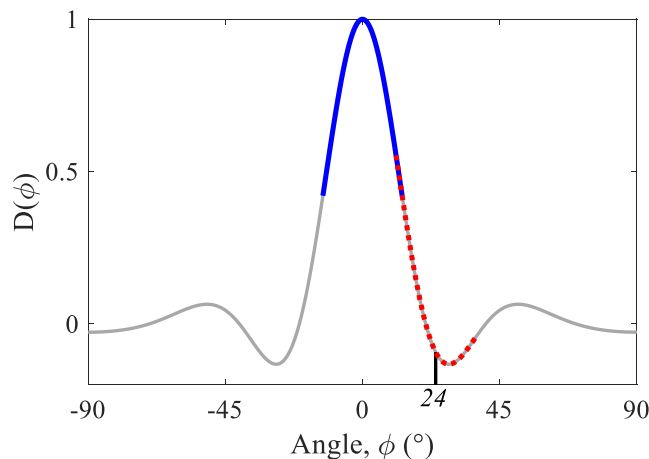
$$359 \quad D(\phi) = \frac{2J_1(kb \sin \phi)}{kb \sin \phi} \quad (9)$$

360 from [24] where  $J_1$  is the 1<sup>st</sup> order Bessel function,  $k$  is the wavenumber,  $b$  is the element radius  
 361 and  $\phi$  is an angle relative to the element normal.  $D(\phi)$  represents the directivity on  
 362 transmission and reception, so to obtain the total directivity for a transmit-receive element pair  
 363 their individual directivities at the respective angles are calculated and multiplied together. The  
 364 array elements' highest sensitivity is at  $0^\circ$ , which corresponds to the direction directly beneath  
 365 the element. For a planar surface parallel to the base of the array, the directivity of the elements  
 366 is therefore the highest, as shown in the  $\pm\theta_c$  range by the solid blue line in Fig. 10. However,  
 367 for a surface inclination of  $24^\circ$ , as shown by the dashed red region of the graph, the directivity  
 368 within the  $24^\circ \pm \theta_c$  range is much lower. For this surface inclination the elements have reduced  
 369 sensitivity to any signals entering or leaving the specimen. The ratio of the average directivity  
 370 in the parallel surface case when compared to the inclined surface case is approximately 20:1.  
 371 By examining BDHs O, P and Q in Fig. 7(c), (d) and (e) respectively, this effect is evident as  
 372 the average amplitude in BDH O is approximately 10 dB lower than that in BDHs P and Q,  
 373 illustrating that defects located under the inclined region have lower amplitudes when

374 compared to defects located under a planar surface parallel to the array. From Fig. 8(a) and (b)  
 375 it can be seen that the true and measured values closely agree for visible defects.



376  
 377 **Fig. 9.** Surface inclination with the locations of the EDM notches and BDHs marked. White circles  
 378 represent defects that were unable to be imaged and white lines represent portions of EDM notches that  
 379 were unable to be imaged.



380  
 381 **Fig. 10.** The directivity of a 1.7 mm diameter circular element radiating into water at 3 MHz as a  
 382 function of angle relative to the element normal direction. The solid blue region is the range  $\pm\theta_c$  and  
 383 the dashed red region is the range  $24^\circ \pm \theta_c$ .

384 The surface spatial resolution was 0.3 mm, which was just below  $\lambda_w$ , and the interior TFM  
 385 spatial resolution was set to  $\lambda_{AI}/4$ , or half of the diffraction limit of the longitudinal wavelength.  
 386 The runtime on a desktop computer for the entire imaging process was 40 hours (Intel Core i7-  
 387 6700 3.4 GHz quad-core processor; 16 GB RAM, Quadro K620 GPU).

## 388 6. Conclusion

389 With the advances in ultrasonic imaging over the past few years, the use of 2D phased arrays  
 390 for volumetric imaging has the potential to open the door to many new imaging applications.  
 391 The use of FMC and TFM in this work has demonstrated the ability of 2D arrays to  
 392 volumetrically image defects through an unknown doubly-curved surface, provided the surface

393 and array orientation is favourable. Defects that were able to be imaged were well focused, but  
394 defects positioned in locations beneath a relatively steep surface inclination were unable to be  
395 imaged for multiple reasons, such as unfavourable orientation of the array and surface, along  
396 with element directivity. The extracted surface profile was in very good agreement with the  
397 true surface as the RMS error between them was 0.40 mm and 95% of absolute error values  
398 were less than 0.07 mm. Although the surface extraction method was successful when  
399 extracting this surface, it does need further investigation as it may not work as well on more  
400 complex surfaces, such as those with discontinuities or very steep interfaces. A possible  
401 solution could involve extracting surface points using the four nearest neighbours around each  
402 point, instead of extracting along 2D planes as was demonstrated here. When considering the  
403 positioning of defects, it was found that the standard deviation of depth and lateral distance  
404 from the surface notch measurements is 0.68 mm and 0.89 mm respectively. This illustrates  
405 that the measured positions of the defects which could be imaged agreed with the true locations.  
406 As the average amplitudes of identical BDHs decreases with increasing surface inclination,  
407 erroneous imaging results may be obtained. The severity of a defect is not taken simply by its  
408 amplitude, so some defects may be missed by thresholding the images at an amplitude level.

409 Future work will involve work on the sizing flat-bottomed holes and round-bottomed holes  
410 through a similar surface profile to simulate the sizing of cracks and voids. A more advanced  
411 stitching method could also be investigated to improve the calculation of amplitudes in  
412 overlapped regions, along with investigating methods of compensating for amplitude scaling  
413 through the use of sensitivity maps. Another investigative avenue could focus on the  
414 optimisation of the imaging algorithm to potentially speed up the computational process.

## 415 Acknowledgement

416 This work was supported by Frazer-Nash Consultancy.

## 417 References

- 418 [1] Lowe MJS, Alleyne DN, Cawley P. Defect detection in pipes using guided waves.  
419 Ultrasonics 1998;36:147–54. [https://doi.org/10.1016/S0041-624X\(97\)00038-3](https://doi.org/10.1016/S0041-624X(97)00038-3).
- 420 [2] Croxford AJ, Wilcox PD, Drinkwater BW, Konstantindis G. Strategies for guided-  
421 wave structural health monitoring. Proc R Soc A 2007;463:2961–81.  
422 <https://doi.org/10.1098/rspa.2007.0048>.
- 423 [3] Pudovikov S, Bulavinov A, Pinchuk R. Innovative ultrasonic testing (UT) of nuclear  
424 components by sampling phased array with 3D visualization of inspection results. 8th  
425 Int. Conf. NDE Relat. to Struct. Integr. Nucl. Press. Components, 2010.
- 426 [4] Amenabar I, Mendikute A, López-Arraiza A, Lizaranzu M, Aurrekoetxea J.  
427 Comparison and analysis of non-destructive testing techniques suitable for  
428 delamination inspection in wind turbine blades. Compos Part B Eng 2011;42:1298–  
429 305. <https://doi.org/10.1016/j.compositesb.2011.01.025>.
- 430 [5] Clark R. Rail flaw detection: overview and needs for future developments. NDT E Int  
431 2004;37:111–8. <https://doi.org/10.1016/j.ndteint.2003.06.002>.
- 432 [6] Wilcox PD, Holmes C, Drinkwater BW. Enhanced defect detection and  
433 characterisation by signal processing of ultrasonic array data. Proc. 9th ECNDT, 2006.
- 434 [7] Drinkwater BW, Wilcox PD. Ultrasonic arrays for non-destructive evaluation: A  
435 review. NDT E Int 2006;39:525–41. <https://doi.org/10.1016/j.ndteint.2006.03.006>.

436 [8] Velichko A, Wilcox PD, Thompson DO, Chimenti DE. Defect characterization using  
437 two-dimensional arrays. *Rev. Prog. Quant. Nondestruct. Eval.*, 2011, p. 835–42.  
438 <https://doi.org/10.1063/1.3591934>.

439 [9] Wilcox PD. Ultrasonic arrays in NDE: Beyond the B-scan. *Rev Prog Quant*  
440 *Nondestruct Eval* 2013;1511:33–50. <https://doi.org/10.1063/1.4789029>.

441 [10] Sun C, Gang T, Peng Y. Ultrasonic phased array three-dimensional imaging using  
442 TFM-based slice. *19th World Conf. Non-Destructive Test.*, 2016.

443 [11] Kerr W, Rowe P, Pierce SG. Accurate 3D reconstruction of bony surfaces using  
444 ultrasonic synthetic aperture techniques for robotic knee arthroplasty. *Comput Med*  
445 *Imaging Graph* 2017;58:23–32. <https://doi.org/10.1016/j.compmedimag.2017.03.002>.

446 [12] Ditchburn RJ, Burke SK, Scala CM. NDT of welds: state of the art. *NDT E Int*  
447 1996;29:111–7. [https://doi.org/10.1016/0963-8695\(96\)00010-2](https://doi.org/10.1016/0963-8695(96)00010-2).

448 [13] Hunter AJ, Drinkwater BW, Wilcox PD. Autofocusing ultrasonic imagery for non-  
449 destructive testing and evaluation of specimens with complicated geometries. *NDT E*  
450 *Int* 2010;43:78–85. <https://doi.org/10.1016/j.ndteint.2009.09.001>.

451 [14] Malkin RE, Franklin AC, Bevan RLT, Kikura H, Drinkwater BW. Surface  
452 reconstruction accuracy using ultrasonic arrays: Application to non-destructive testing.  
453 *NDT E Int* 2018;96:26–34. <https://doi.org/10.1016/j.ndteint.2018.03.004>.

454 [15] Le Jeune L, Robert S, Dumas P, Membre A, Prada C. Adaptive ultrasonic imaging  
455 with the total focusing method for inspection of complex components immersed in  
456 water. *Rev. Prog. Quant. Nondestruct. Eval.*, Boise, Idaho: 2015, p. 1037–46.  
457 <https://doi.org/10.1063/1.4914712>.

458 [16] Tweedie A, O’Leary RL, Harvey G, Gachagan A, Holmes C, Wilcox PD, et al. Total  
459 focussing method for volumetric imaging in immersion non destructive evaluation.  
460 2007 IEEE Ultrason. Symp. Proc., IEEE; 2007, p. 1017–20.  
461 <https://doi.org/10.1109/ULTSYM.2007.259>.

462 [17] Drinkwater BW, Bowler AI. Ultrasonic array inspection of the Clifton Suspension  
463 Bridge chain-links. *Insight - Non-Destructive Test Cond Monit* 2009;51:491–8.  
464 <https://doi.org/10.1784/insi.2009.51.9.491>.

465 [18] Russell J, Long R, Cawley P. Development of a twin crystal membrane coupled  
466 conformable phased array for the inspection of austenitic welds. *Rev Prog Quant*  
467 *Nondestruct Eval* 2011;30:811–8. <https://doi.org/10.1063/1.3591931>.

468 [19] Roy O, Mahaut S, Casula O. Control of the ultrasonic beam transmitted through an  
469 irregular profile using a smart flexible transducer: modelling and application.  
470 *Ultrasonics* 2002;40:243–6. [https://doi.org/10.1016/S0041-624X\(02\)00145-2](https://doi.org/10.1016/S0041-624X(02)00145-2).

471 [20] Casula O, Poidevin C, Cattiaux G, Fleury G. A flexible phased array transducer for  
472 contact examination of components with complex geometry. *Proc. 16th World Conf.*  
473 *NDT*, 2004.

474 [21] Holmes C, Drinkwater BW, Wilcox PD. Post-processing of the full matrix of  
475 ultrasonic transmit–receive array data for non-destructive evaluation. *NDT E Int*  
476 2005;38:701–11. <https://doi.org/10.1016/j.ndteint.2005.04.002>.

477 [22] Schuster A. *An introduction to the theory of optics*. 1909.



- 478 [23] Bevan RLT, Zhang J, Budyn N, Croxford AJ, Wilcox PD. Experimental quantification  
479 of noise in linear ultrasonic imaging. IEEE Trans Ultrason Ferroelectr Freq Control  
480 2019;66:79–90. <https://doi.org/10.1109/TUFFC.2018.2874720>.
- 481 [24] Kinsler LE, Frey AR, Coppens AB, Sanders J V. Fundamentals of acoustics. 4th  
482 editio. John Wiley & Sons; 2000.

## 483 Appendix

484 An outline of the imaging process is given below. For the data presented in this paper, the  
485 average number of ray paths calculated to generate a single 3D TFM image for an individual  
486 array position over both imaging stages was approximately 41 billion. Due to this large amount  
487 of computationally-intensive calculations required and the independent nature of the TOF and  
488 TFM image calculations, the parallel computing platform CUDA was used to provide a huge  
489 processing speed up on the graphics processing unit (GPU).

490 (M) represents calculations in MATLAB on the central processing unit (CPU) and (C)  
491 represents calculations using CUDA on the GPU.

- 492 1. Initialise the scanning tank by mounting and orientating the array parallel to the back  
493 wall of the specimen using a B-scan image. Calculate velocities of sound in water and  
494 the specimen material.
- 495 2. Scan over the entire surface of the specimen in increments equal to half of the diameter  
496 of the active region of the array, collecting an FMC dataset at each array position.
- 497 3. (M) Load all FMC datasets, filter time-data and define imaging parameters.
- 498 4. (C) Calculate TOFs for the surface region at each array position and generate single-  
499 medium 3D TFM images using each FMC dataset and the velocity of sound in water.  
500 [section 3.1]

501 [The output for  $N$  array positions is  $N$  3D surface TFM images.]

- 502 5. (M) Stitch  $N$  surface TFM images into a stitched 3D TFM image of the entire surface.
- 503 6. (M) Extract surface points from stitched TFM image. [section 3.1]

504 [Output is  $(x, y, z)$  coordinates of the extracted surface.]

- 505 7. (M) Define a subset of the point cloud of extracted surface points for each array position  
506 and define interior imaging parameters.
- 507 8. (C) Calculate TOFs through the surface points for each FMC dataset and generate  
508 immersion 3D TFM images for each array position while compensating for the  
509 velocities of sound in each medium. [section 3.2]

510 [The output for  $N$  array positions is  $N$  3D interior TFM images.]

- 511 9. Stitch  $N$  interior TFM images into a stitched 3D TFM image of the interior of the  
512 specimen.